



Imaging local discharge cascades for correlated electrons in WS_2/WSe_2 moiré superlattices

Hongyuan Li^{1,2,3,9}, Shaowei Li^{1,3,4,5,9}✉, Mit H. Naik^{1,3}, Jingxu Xie¹, Xinyu Li¹, Emma Regan^{1,2,3}, Danqing Wang^{1,2}, Wenyu Zhao¹, Kentaro Yumigeta⁶, Mark Blei⁶, Takashi Taniguchi⁷, Kenji Watanabe⁸, Sefaattin Tongay⁶, Alex Zettl^{1,3,4}, Steven G. Louie^{1,3}, Michael F. Crommie^{1,3,4}✉ and Feng Wang^{1,3,4}✉

Transition metal dichalcogenide moiré heterostructures provide an ideal platform to explore the extended Hubbard model¹, where long-range Coulomb interactions play a critical role in determining strongly correlated electron states. This has led to experimental observations of Mott insulator states at half filling^{2–4} as well as a variety of extended Wigner crystal states at different fractional fillings^{5–9}. However, a microscopic understanding of these emerging quantum phases is still lacking. Here we describe a scanning tunnelling microscopy (STM) technique for the local sensing and manipulation of correlated electrons in a gated WS_2/WSe_2 moiré superlattice, which enables the experimental extraction of fundamental extended Hubbard model parameters. We demonstrate that the charge state of the local moiré sites can be imaged by their influence on the STM tunnelling current. In addition to imaging, we are also able to manipulate the charge state of correlated electrons. When we ramp the bias on the STM tip, there is a local discharge cascade of correlated electrons in the moiré superlattice, which allows us to estimate the nearest-neighbour Coulomb interaction. Two-dimensional mapping of the moiré electron charge states also enables us to determine the on-site energy fluctuations at different moiré sites. Our technique should be broadly applicable to many semiconductor moiré systems, offering a powerful tool for the microscopic characterization and control of strongly correlated states in moiré superlattices.

Transition metal dichalcogenide (TMD) moiré heterostructures provide a platform for exploring strongly correlated physics in the extended Hubbard model^{1–9}. Compared with graphene-based moiré heterostructures, semiconductor TMD heterostructures feature stronger long-range Coulomb interactions and flatter moiré minibands, thus leading to new emergent correlated electronic states that are absent in graphene-based moiré systems^{10–15}. Indeed, several recent studies have revealed correlated states in TMD moiré superlattices, including charge-transfer insulator states^{16,17} and a rich variety of extended Wigner crystal states at fractional fillings^{5–8}. Direct local characterization of the correlated states and physical parameters of the extended Hubbard model in TMD moiré

heterostructures, however, have so far been lacking. For example, little is known about the strength of the nearest-neighbour electron–electron interactions or the magnitude of inhomogeneity in on-site energies within TMD moiré superlattices.

Here we describe a new scanning tunnelling microscopy (STM)-based technique for imaging and manipulating the charge states of correlated electrons in gated WS_2/WSe_2 moiré superlattices that enables the determination of nearest-neighbour Coulomb interaction energies and on-site energy fluctuations. Using this, we are able to image the charge state of moiré sites via their influence on the tunnelling current between an STM tip and the WS_2/WSe_2 heterostructure. By combining a back-gate voltage with the STM bias, this mechanism enables us to locally charge and discharge correlated moiré electrons. Gradually ramping the STM bias under these conditions results in a cascade of discharging events for correlated electrons at multiple neighbouring moiré sites. The investigation of this discharge cascade allows us to determine the nearest-neighbour Coulomb interactions as well as on-site energy fluctuations within the moiré superlattice.

A schematic of our aligned WSe_2/WS_2 heterostructure device is shown in Fig. 1a. We used an array of graphene nanoribbons with ~100–200 nm separation as a top contact electrode and doped silicon substrate as a back gate to control the global carrier density within the heterostructure. Details of fabrication and low-temperature operation of the device are presented in ref. 18. Figure 1b shows an ultrahigh-vacuum STM image of the moiré superlattice in an exposed WSe_2/WS_2 area between two graphene nanoribbons at temperature $T = 5.4$ K. Three types of moiré site are labelled: AA, $B^{Se/W}$ and $B^{W/S}$, with the corresponding chemical structures shown in the top-view sketch in Fig. 1c. The moiré period $l_m = 8.1$ nm, indicating a near-zero twist angle.

We characterized our gated WSe_2/WS_2 heterostructure via scanning tunnelling spectroscopy. Figure 1d,f shows the plots of differential conductivity (dI/dV) at the $B^{Se/W}$ and $B^{W/S}$ sites, respectively, as a function of both STM tip bias V_b and back-gate voltage V_g (I is the tunnelling current). Here we focus on the electron-doped regime of the moiré heterostructure at positive V_g , with the Fermi level located in the conduction band. The dI/dV spectra show a negligible signal

¹Department of Physics, University of California at Berkeley, Berkeley, CA, USA. ²Graduate Group in Applied Science and Technology, University of California at Berkeley, Berkeley, CA, USA. ³Materials Sciences Division, Lawrence Berkeley National Laboratory, Berkeley, CA, USA. ⁴Kavli Energy NanoScience Institute at the University of California Berkeley and the Lawrence Berkeley National Laboratory, Berkeley, CA, USA. ⁵Department of Chemistry and Biochemistry, University of California at San Diego, La Jolla, CA, USA. ⁶School for Engineering of Matter, Transport and Energy, Arizona State University, Tempe, AZ, USA. ⁷International Center for Materials Nanoarchitectonics, National Institute for Materials Science, Tsukuba, Japan. ⁸Research Center for Functional Materials, National Institute for Materials Science, Tsukuba, Japan. ⁹These authors contributed equally: Hongyuan Li, Shaowei Li. ✉e-mail: shaoweili@ucsd.edu; crommie@berkeley.edu; fengwang76@berkeley.edu

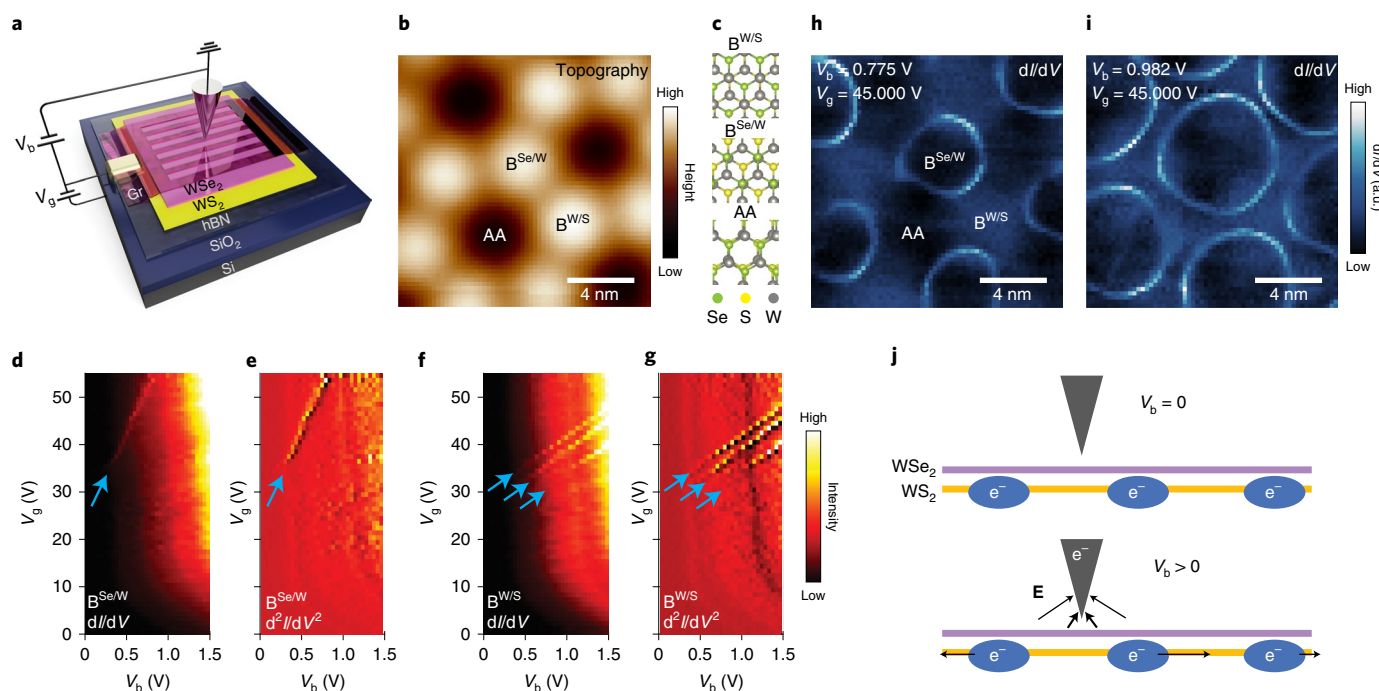


Fig. 1 | Local discharging of electrons at moiré sites by an STM tip. **a**, Schematic of the gate-tunable WSe_2/WS_2 heterostructure device used for this STM study. Graphene nanoribbons (Gr) are placed on top of WSe_2/WS_2 as the contact electrodes. **b**, STM image of an exposed WSe_2/WS_2 area ($T = 5.4\text{ K}$). A moiré superlattice is clearly resolved. Here $V_b = -3\text{ V}$, $I = 100\text{ pA}$ and $V_g = 45\text{ V}$. **c**, Schematic of the three high-symmetry stacking configurations: $\text{B}^{\text{W/S}}$, $\text{B}^{\text{Se/W}}$ and AA. **d–g**, Gate-dependent dI/dV spectra measured at the $\text{B}^{\text{Se/W}}$ (**d**) and $\text{B}^{\text{W/S}}$ (**f**) site. Bright dispersive features labelled by blue arrows correspond to the tip-induced charging/discharging of electrons at adjacent $\text{B}^{\text{Se/W}}$ moiré sites. To highlight the dispersive feature, the corresponding second-order derivative (d^2I/dV^2) spectra are plotted in **e** and **g**, respectively. **h, i**, The dI/dV maps of the region shown in **b** measured with $V_b = 0.775\text{ V}$ and $V_g = 45.000\text{ V}$ (**h**) and $V_b = 0.982\text{ V}$ and $V_g = 45.000\text{ V}$ (**i**). The tip-sample distance for the dI/dV mappings is controlled by the following set points: $V_b = -3\text{ V}$, $I = 100\text{ pA}$. Discharge of the moiré electron causes a dI/dV mapping, which appears as a circular ring surrounding each $\text{B}^{\text{Se/W}}$ site in the moiré superlattice. The periodic discharging rings expand with V_b . **j**, Sketch of the tip-induced moiré electron discharging. The STM tip acts as a local top gate that modifies the electron energy at nearby $\text{B}^{\text{Se/W}}$ moiré sites and discharges them for bias voltages greater than a local threshold value.

for $0 < V_b < 0.4\text{ V}$ due to a very small tunnelling probability to the conduction band edge states, which lie at the K point of the bottom WS_2 layer and that feature a large out-of-plane decay constant^{18,19}. At $V_b > 0.4\text{ V}$, the tip electrons can more readily tunnel into the Q-point states of the conduction band, which protrude further into the vacuum.

In addition to a general increase in the dI/dV signal for $V_b > 0.4\text{ V}$, we observe sharp dispersive dI/dV peaks at different moiré sites (the bright features labelled by blue arrows in Fig. 1d,f). These dispersive peaks can be more clearly observed in the density plot of the second-order derivative (d^2I/dV^2), as shown in Fig. 1e,g. To better understand the origin of these peaks, we performed two-dimensional dI/dV mapping at $V_b = 0.775\text{ V}$ (Fig. 1h) and $V_b = 0.982\text{ V}$ (Fig. 1i) for a fixed $V_g = 45.000\text{ V}$. In these images, the dispersive dI/dV peaks (Fig. 1d,f) correspond to periodic circular rings surrounding the $\text{B}^{\text{Se/W}}$ sites that expand as V_b increases. This behaviour can be explained by discrete charging and discharging events for localized moiré electrons at the $\text{B}^{\text{Se/W}}$ sites, controlled by the application of V_g and V_b . The STM tip plays two roles in the discharging events: (1) it acts as a source electrode for the tunnelling current between the tip and heterostructure, thereby injecting electrons into the excited states of the conduction band; (2) it acts as a local gate that can change the charge state of the conduction band edge states localized at the $\text{B}^{\text{Se/W}}$ moiré sites (Supplementary Fig. 1 provides more details). The gain or loss of an electron at a $\text{B}^{\text{Se/W}}$ moiré site modifies the electron tunnelling rate between the STM tip and heterostructure surface due to the resultant change in Coulomb potential. Charging and discharging events at the

$\text{B}^{\text{Se/W}}$ sites thus lead to a corresponding jump in the STM tunnelling current and result in sharp peaks in the dI/dV spectra. A similar ring-like charging behaviour has been seen via STM in other nanoscale systems^{20–24}.

Ab initio calculations show that the WSe_2/WS_2 moiré flat band states at the conduction band edge are strongly localized at the $\text{B}^{\text{Se/W}}$ sites in real space (Supplementary Fig. 2). For $V_g > 25\text{ V}$, the moiré global filling factor n/n_0 is greater than 1, where n is the gate-controlled carrier density and n_0 is the carrier density corresponding to a half-filled moiré miniband with one electron per moiré lattice site. At this gate voltage, there is, therefore, at least one electron localized at each $\text{B}^{\text{Se/W}}$ site. At a positive sample bias V_b , negative charge accumulates at the tip and repels nearby electrons, thus causing the electrons localized to the $\text{B}^{\text{Se/W}}$ sites to discharge when V_b exceeds a threshold value (schematic shown in Fig. 1j). The efficiency with which the STM tip discharges nearby localized electrons sensitively depends on their distance to the tip and thus results in circular discharging rings for a given V_b (Fig. 1h). These rings continuously expand with increased V_b since a larger V_b enables the discharge of localized electrons at larger tip–electron distances (Fig. 1i). When the tip is inside a discharge ring, the circled moiré site is empty, whereas it contains an electron when the tip is outside the ring.

The STM tip can discharge multiple correlated electrons at neighbouring moiré sites in a cascade fashion with increased V_b , thus providing a tool to probe electron correlation in moiré systems. We have systematically examined the discharge cascade of correlated electrons in a WSe_2/WS_2 flat band by performing

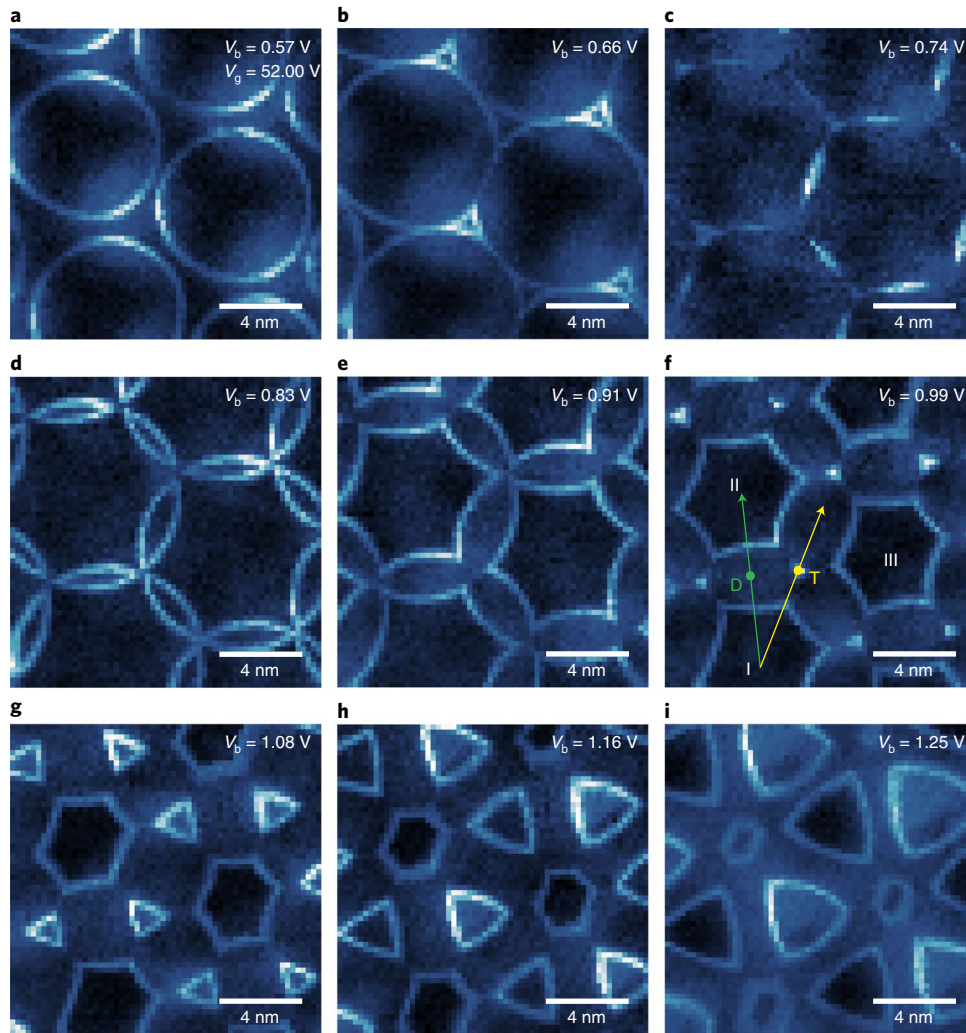


Fig. 2 | Discharging correlated electrons. **a–i**, Evolution of moiré discharging rings with increasing V_b (V_g fixed at 52 V): $V_b = 0.57$ V (**a**), $V_b = 0.66$ V (**b**), $V_b = 0.74$ V (**c**), $V_b = 0.83$ V (**d**), $V_b = 0.91$ V (**e**), $V_b = 0.99$ V (**f**), $V_b = 1.08$ V (**g**), $V_b = 0.66$ V (**h**) and $V_b = 1.25$ V (**i**). The rings expand with increased V_b , and intricate new patterns emerge when they cross each other. These complex patterns indicate discharging cascades of multiple correlated electrons in neighbouring moiré sites. The dI/dV spectra along the green and yellow lines in **f** are shown in Fig. 3. Here D and T denote the two-ring and three-ring crossing points, respectively. The dI/dV mapping set points are as follows: $V_b = -3$ V, $I = 100$ pA, $V_g = 52$ V, $T = 5.4$ K.

two-dimensional dI/dV mapping of the moiré pattern as a function of V_b . Figure 2a–i shows the evolution of discharge rings as V_b is increased from 0.57 V to 1.25 V for fixed $V_g = 52.00$ V. The discharge rings expand with increased V_b and begin crossing each other at $V_b = 0.66$ V. Near the crossing point, the STM tip effectively couples to multiple adjacent moiré sites and can generate a cascade of discharging events. Patterns emerge as the rings cross each other with increasing V_b , and these differ from a simple superposition of ever-increasing rings as expected from a non-interacting picture, thus providing a manifestation of electron correlation in TMD moiré superlattices.

The effects of electron correlation on cascade discharging can be more effectively visualized in position-dependent dI/dV spectra. Figure 3a shows the position-dependent dI/dV spectra along the green line in Fig. 2f. This line passes through a high-symmetry two-ring crossing point (marked as D), which is equidistant to neighbouring $B^{\text{Se/W}}$ sites I and II. For positions near D, sites I and II are occupied at low V_b (that is, $n = 2$, where n is the total electron count for the adjacent moiré sites). As V_b increases, however, the tip successively discharges the two sites and n changes from 2 to 1 and then from 1 to 0 as V_b crosses two dI/dV discharge peaks.

At D, one would expect—by symmetry—that these two discharging events should occur at the same value of V_b for a non-interacting picture. The data in Fig. 3a, however, show that these two discharging events occur at different V_b values, with a discharging gap of $\Delta V_b^D = 122 \pm 9$ mV (obtained via high-resolution dI/dV mapping; Supplementary Fig. 4).

A similar behaviour can be seen at another high-symmetry point, marked as T in Fig. 2f. Here the STM tip is equidistant to three neighbouring $B^{\text{Se/W}}$ sites marked as I, II and III; therefore, the discharge cascade involves three electrons. Figure 3e shows the position-dependent dI/dV spectra along the yellow line in Fig. 2f, which passes through T. Three dI/dV peaks are seen in the spectra, corresponding to a cascade of three discharging events that decrease the total number of electrons (n) in sites I–III from 3 to 2 to 1 and finally to 0. At T, we observe the voltage difference between the 3→2 and 2→1 discharge peaks to be identical to the difference between the 2→1 and 1→0 discharge peaks within the uncertainty of our measurement: $\Delta V_b^T = 166 \pm 11$ mV.

To interpret the discharge cascade of correlated electrons in our TMD moiré system in terms of physically important parameters, we employ a simplified N -moiré-site model that includes on-site and

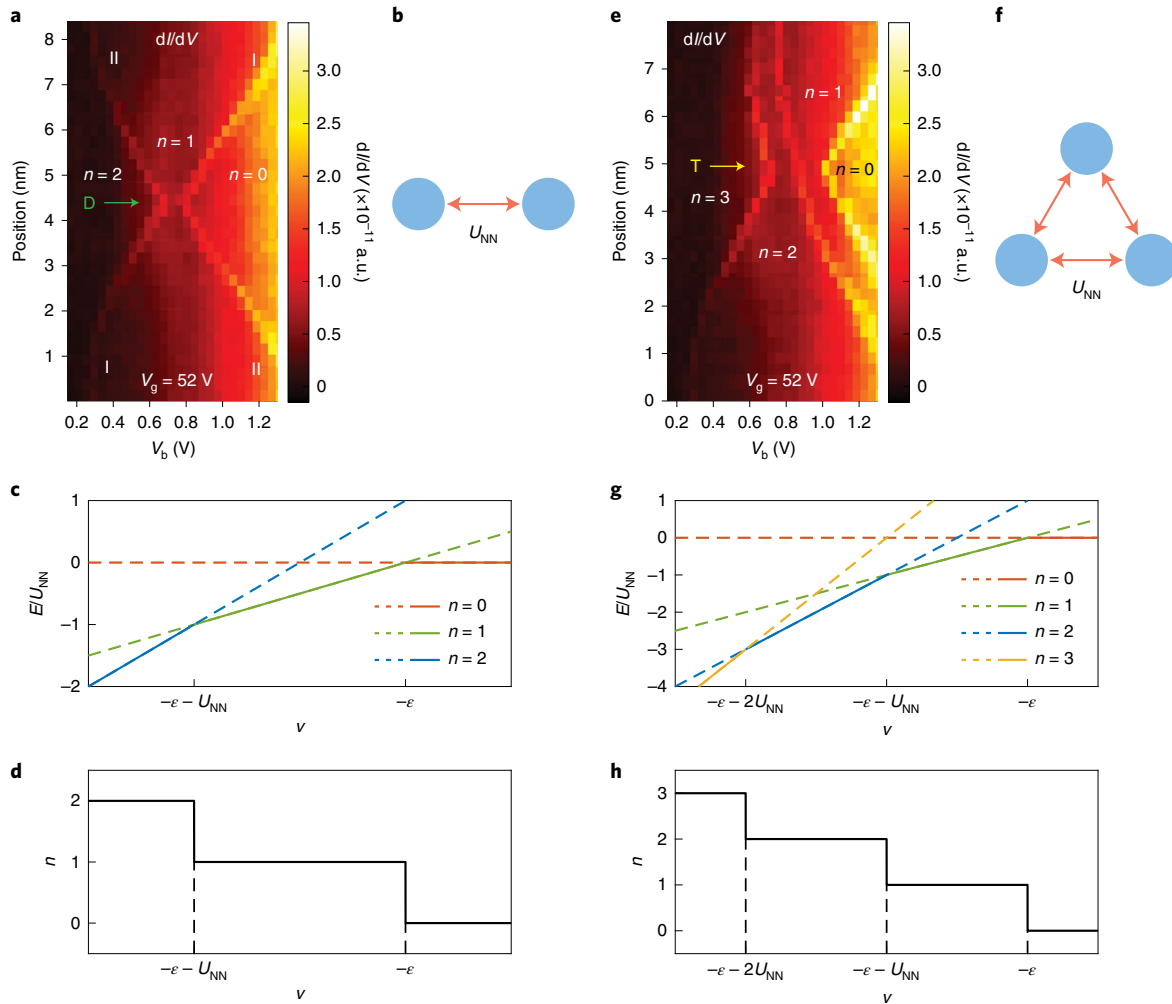


Fig. 3 | Correlation effects on cascade discharging of moiré sites. **a**, Position-dependent dI/dV spectra along the green line shown in Fig. 2f, which passes through D. The dI/dV peaks indicated by bright lines correspond to discharging events where the total electron number decreases from 2 to 1 and from 1 to 0 from left to right. Also, I and II indicate the moiré sites being discharged as labelled in Fig. 2f. **b**, Sketch of a simplified two-site cluster model for analysis of discharge behaviour at D. Here U_{NN} indicates the nearest-neighbour Coulomb interaction. **c,d**, Calculated energy levels (**c**) and total electron number (**d**) of cluster ground state as a function of v (**d**) for the two-site model. States with different electron numbers are labelled by colour. The discrete changes in n in **d** correspond to discharge peaks at B. **e**, Position-dependent dI/dV spectra along the yellow line shown in Fig. 2f. This linecut passes through T. Bright lines indicate discharging events at three distinct bias voltages. **f**, Sketch of a simplified three-site cluster model for analysis of the discharge behaviour at T. **g,h**, Calculated energy levels (**g**) and total electron number of cluster ground state as a function of v (**h**) for the three-site model.

nearest-neighbour interactions. The Hamiltonian describing our system is

$$H = \sum_{i=1}^N (\epsilon_i + v_i) n_i + \frac{1}{2} U_{NN} \sum_{\langle ij \rangle} n_i n_j. \quad (1)$$

Here U_{NN} is the nearest-neighbour Coulomb interaction term, $\langle ij \rangle$ sums only over the nearest neighbours and N represents the number of moiré sites close to the tip (equals to 2 or 3 in our system). Further, n_i is the electron number at moiré site i , ϵ_i is the on-site energy at site i and v_i is the potential energy shift induced by V_b and V_g at site i . Here v_i has the form

$$v_i = \alpha_i e V_b - \beta_i e V_g \quad (2)$$

where $e = 1.6 \times 10^{-19} \text{C}$, and α_i and β_i are dimensionless coefficients describing the electrostatic potential at site i induced by V_b and V_g , respectively. We note that α_i sensitively depends on the tip

position r_i , implying $\alpha_i = \alpha_i(r_i)$. In this model, we neglect intersite hopping due to the small bandwidth of the moiré flat band ($\sim 5 \text{ meV}$; Supplementary Fig. 3). We also ignore the on-site Coulomb interactions, since the total number of electrons for sites near the tip is smaller than N and the energy of double occupancy for a single site is assumed to be prohibitively large. This Hamiltonian describes electrons in the lowest conduction band near the tip since higher-energy delocalized electrons are assumed to be swept away by tip repulsion for $V_b > 0$.

Our strategy for understanding the discharge phenomena observed here is to explore the consequences of this Hamiltonian for different electron occupation values n . By comparing the different total energies $E(n)$, we can identify the charge occupation n^* , which has the lowest total energy and we assume that this is the ground state. A discharge event from the $n = n^* + 1$ state to the $n = n^*$ state occurs when $E(n^*) < E(n^* + 1)$. As our measurements primarily involve discharging events, the largest relevant energy is U_{NN} , which is larger than the energy associated with intersite hopping. As a result, the behaviour induced by equation (1) can be

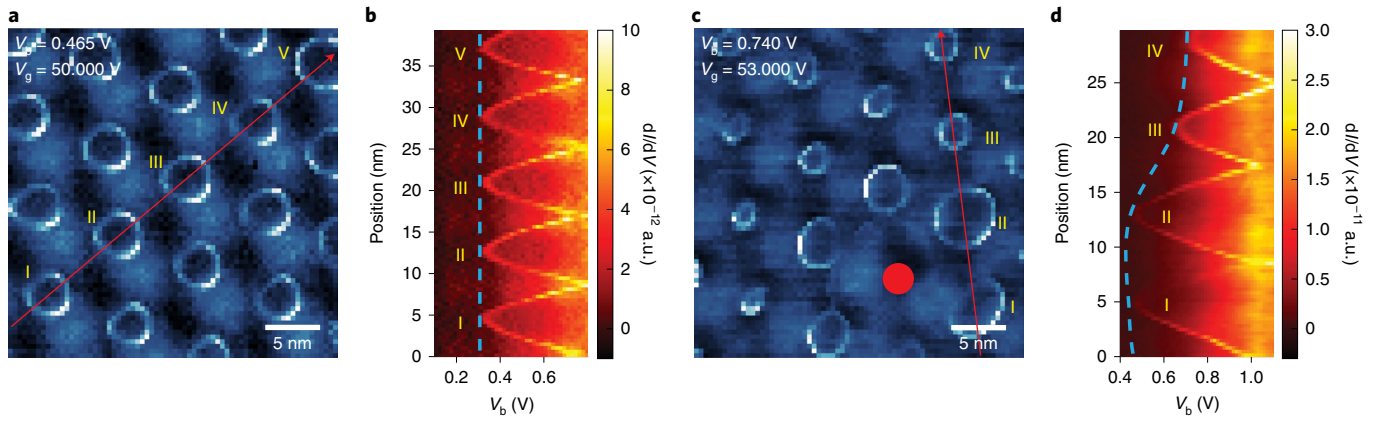


Fig. 4 | Inhomogeneity of moiré on-site energy. **a**, The dI/dV map of a representative homogeneous region of the WS_2/WS_2 moiré superlattice ($V_b = 0.465$ V, $V_g = 50.000$ V). **b**, The dI/dV spectra measured along the red linecut shown in **a**. Discharge voltages at moiré sites I–IV are seen to be nearly uniform. **c**, The dI/dV map of the discharge rings close to a point defect shows strongly non-uniform behaviour. The solid red circle marks the position of the point defect ($V_b = 0.740$ V, $V_g = 53.000$ V). The defect concentration is roughly of the order of 10^{10} cm $^{-2}$. **d**, The dI/dV spectra measured along the red linecut shown in **c**. A notable reduction in discharge bias is observed for sites I and II near the defect. The tip–sample distance is determined by the following mapping set points: $V_b = -3$ V, $I = 100$ pA.

treated within an essentially classical framework that is adequate to extract information on the Hubbard model parameters ϵ_i and U_{NN} from our data, which is the main goal of this work.

We start by applying this model to analyse the discharge behaviour that occurs when the STM tip is held at position D. Here the tip is equidistant from sites I and II; therefore, we model the moiré system as an $N=2$ cluster, as illustrated in Fig. 3b. The on-site energy (equation (1)) for sites I and II can be written as ϵ and the electrostatic potential energy (equation (2)) for each site is $\nu = e\alpha(r^D)V_b - e\beta V_g$, where $r^D = 3.9$ nm is equidistant from sites I and II. Straightforward energetic considerations allow the $N=2$ ground-state energy for different n values to be written as $E(n=2) = 2(\epsilon + \nu) + U_{NN}$, $E(n=1) = \epsilon + \nu$ and $E(n=0) = 0$. Figure 3c shows a plot of $E(2)$, $E(1)$ and $E(0)$ as a function of the applied electrostatic potential (ν). Three different regimes can be seen, where the ground-state energy transitions from an $n=2$ charge state to an $n=1$ charge state and then to an $n=0$ charge state as ν is increased, and the boundaries between them are electron-discharging events. The first happens when $E(2) = E(1)$, which occurs at the potential $\nu_1 = -U_{NN} - \epsilon$. The second happens when $E(1) = E(0)$, which occurs at the potential $\nu_2 = -\epsilon$. The difference in electrostatic potential energy between these two discharge events is then $\Delta\nu = \nu_2 - \nu_1 = U_{NN}$. Using equation (2) and assuming that the gate voltage remains unchanged while ramping the bias voltage (typical for our experiments) allows U_{NN} to be expressed in terms of the first and second discharge bias voltages: $U_{NN} = e\alpha(r^D)(V_{b2} - V_{b1}) = e\alpha(r^D)\Delta V_b^D$, where ΔV_b^D is the bias voltage difference between discharge events at D.

When the tip is located at T, the discharge cascade behaviour can be analysed using similar reasoning, except for an $N=3$ cluster instead of an $N=2$ cluster. In this case, $\nu = e\alpha(r^T)V_b - e\beta V_g$, where $r^T = 4.7$ nm is the distance between T and the three neighbouring $B^{Se/W}$ sites. The resulting energy levels for different n values are found to be $E(3) = 3(\epsilon + \nu) + 3U_{NN}$, $E(2) = 2(\epsilon + \nu) + U_{NN}$, $E(1) = \epsilon + \nu$ and $E(0) = 0$, which are plotted in Fig. 3g. Discharging events in the three-site moiré system thus occur at $\nu_1 = -\epsilon - 2U_{NN}$, $\nu_2 = -\epsilon - U_{NN}$ and $\nu_3 = -\epsilon - U_{NN}$ (Fig. 3h). This provides an additional means of finding the nearest-neighbour Coulomb interaction energy $U_{NN} = \nu_3 - \nu_2 = \nu_2 - \nu_1 = \alpha(r^T)e\Delta V_b^T$ by utilizing the voltage difference ΔV_b^T between the discharge events at T.

A similar analysis can be used to determine variations in the Hubbard on-site energy, ϵ_i , for a moiré superlattice. This comes from the fact that for small V_b , the STM tip can only discharge

a single moiré site whose energy is described by $E(1) = \epsilon + \nu$ and $E(0) = 0$ (that is, the $N=1$ limit). In this case, discharge happens when $E(1) = E(0)$, which occurs when $\nu = -\epsilon$. Fluctuations in ϵ are thus directly related to fluctuations in the discharge potential, $\delta\epsilon = -\delta\nu$, which (using equation (2)) leads to $\delta\epsilon = -e\alpha(r_i)\delta V_b$, where δV_b represents spatial fluctuations in the measured single-site discharge voltage.

This type of behaviour can be experimentally seen, as shown in Fig. 4. Figure 4a shows a dI/dV map of a pristine region of the WSe_2/WS_2 moiré superlattice for $V_g = 50.000$ V and $V_b = 0.465$ V. The discharge rings around the $B^{Se/W}$ moiré sites are quite uniform in this defect-free region. This uniformity is also seen in a dI/dV spectral linecut (Fig. 4b) that goes through five moiré sites along the red line shown in Fig. 4a. Figure 4c, on the other hand, shows a dI/dV map obtained near a point defect (marked by a red dot) for a similar set of parameters ($V_g = 53.000$ V and $V_b = 0.740$ V). Here the discharge rings are highly non-uniform (the defect moiré site itself does not show a clear discharge ring for this set of parameters due to the large change in its on-site energy). The magnitude of the effect of the defect on neighbouring moiré sites can be seen through the dI/dV spectra (Fig. 4d) obtained along the red linecut shown in Fig. 4c. As shown in Fig. 4d, the defect causes notable changes in the on-site energies of adjacent moiré sites. The discharge bias (measured at the discharge ring centre, namely, $r_i = 0$) of sites I and II, for example, is approximately 200 mV lower than those for sites III and IV (the blue dashed line in Fig. 4d). This implies that the on-site energy shift at sites I and II is $\delta\epsilon \approx \alpha(0)$ (200 meV).

A problem with our characterization of moiré Hubbard parameters up to now is that we cannot convert them to quantitative energies until we determine $\alpha(r_i)$, the geometric electrostatic conversion factor of equation (2). In particular, we require $\alpha(r^D)$, $\alpha(r^T)$ and $\alpha(0)$ to quantitatively determine U_{NN} and $\delta\epsilon$. We can gain some experimental insight into the behaviour of $\alpha(r_i)$ from the slopes of lines representing the discharge peaks in the dI/dV plots of Fig. 1d,e. The condition for discharge in these plots is $\nu = \alpha(r_i)eV_b - \beta eV_g = -C$, where C is a constant independent of V_b and V_g . This can be rewritten as $V_g = \frac{\alpha(r_i)}{\beta}V_b + \frac{C}{e\beta}$, which defines the linear discharge traces observed in Fig. 1d,e. The experimental slope of the discharge traces thus yields the ratio $\frac{\alpha(r_i)}{\beta}$. This does not provide the precise value of $\alpha(r_i)$ (since the back-gate factor β is still unknown), but by assuming that β is constant, we can experimentally determine the proportionality of $\alpha(r_i)$ for different tip locations from the slopes of the

discharge traces at those locations. We have done this for points D, T and B^{se/w}, thereby enabling us to determine the ratios $\alpha(r^D):\alpha(r^T):\alpha(0) = 0.53:0.39:1.00$ (Supplementary Fig. 5).

Obtaining a quantitative value of $\alpha(r_i)$, however, remains difficult since the magnitudes of $\alpha(r_i)$ and β depend on non-universal details of the experimental setup, for example, capacitive coupling between the tip, back gate and different layers of our device heterostructure. To overcome this problem, we utilized the COMSOL 5.3 software package to numerically solve the Poisson's equation for our specific device geometry (Supplementary Fig. 5). Modelling our STM tip as a metallic cone with a cone angle of 30° and a tip–surface height of 0.8 nm results in a ratio of $\alpha(r^D):\alpha(r^T):\alpha(0) = 0.55:0.49:1.00$, which is in reasonable agreement with the experimental ratios mentioned above. A important benefit of the numerical simulation is that it provides the absolute magnitude of the $\alpha(r_i)$ factors: $\alpha(r^D) = 0.18$, $\alpha(r^T) = 0.16$ and $\alpha(0) = 0.33$. These factors allow us to extract a quantitative value of $U_{\text{NN}} = 22 \pm 2$ meV from our measurements at D and $U_{\text{NN}} = 27 \pm 2$ meV from our measurements at T. These two values of U_{NN} are in reasonable agreement with each other, a self-consistency check that helps to validate our overall approach. We are also able to determine the fluctuation in the on-site energy of sites I and II around the point defect in Fig. 4c to be $\delta\epsilon \approx 65$ meV.

The expected value of U_{NN} can be roughly estimated by considering the energy difference associated with the initial position (\mathbf{r}_i) of the discharging electron and its final position (\mathbf{r}_f) after discharge. For an electron being discharged from the $N=2$ cluster discussed above for point D, the initial electrostatic energy is $E(\mathbf{r}_i) \approx \frac{1}{4\pi\epsilon_{\text{eff}}\epsilon_0} \times \frac{e^2}{l_m}$ (assuming each moire site contains one electron). To discharge, an electron needs to escape only the screening distance from the STM tip. Although the screening distance is difficult to accurately determine, since only two lattice sites participate in the discharge events at D (Fig. 3a), we can estimate it to be of the order of l_m . An electron thus only needs to hop a distance of the order of l_m to escape, thus placing the electron in some final configuration with a residual Coulomb energy of the order of $\frac{e^2}{\eta l_m}$, where ηl_m is the distance of the escaped electron from the remaining electron. For $\eta \approx 2$, the electron's energy difference is then $U_{\text{NN}} = E(\mathbf{r}_i) - E(\mathbf{r}_f) \approx \frac{1}{4\pi\epsilon_{\text{eff}}\epsilon_0} \times \left(\frac{e^2}{l_m} - \frac{e^2}{2l_m} \right) = \frac{1}{4\pi\epsilon_{\text{eff}}\epsilon_0} \times \frac{e^2}{2l_m}$.

Here the effective dielectric constant is $\epsilon_{\text{eff}} = \frac{1}{2}(\epsilon_{\text{vac}} + \epsilon_{\text{hBN}})$, where $\epsilon_{\text{vac}} = 1$ is the dielectric constant of vacuum and ϵ_{hBN} is the dielectric constant of hexagonal boron nitride (hBN). Since the dielectric constant of hBN is anisotropic, we approximate it as $\epsilon_{\text{hBN}} = \frac{1}{2}(\epsilon_{\perp} + \epsilon_{\parallel})$ where $\epsilon_{\perp} = 4$ and $\epsilon_{\parallel} = 7$ are the out-of-plane and in-plane dielectric constants of hBN, respectively²⁵.

Taken together, these parameters yield an expected value of $U_{\text{NN}} \approx 30$ meV, which is reasonably consistent with our experimental value of $U_{\text{NN}} \approx 25$ meV obtained by averaging the U_{NN} values measured at D and T. We note that this value of U_{NN} is much larger than the bandwidth $W \approx 5$ meV obtained from ab initio calculations of the conduction miniband for WSe₂/WS₂ moiré heterostructures (Supplementary Fig. 3). This confirms that WSe₂/WS₂ heterostructures lie in the strongly correlated limit, consistent with previous observations of the extended Wigner crystal states in TMD moiré superlattices^{5–8}.

Online content

Any methods, additional references, Nature Research reporting summaries, source data, extended data, supplementary

information, acknowledgements, peer review information; details of author contributions and competing interests; and statements of data and code availability are available at <https://doi.org/10.1038/s41567-021-01324-x>.

Received: 16 February 2021; Accepted: 13 July 2021;

Published online: 16 August 2021

References

- Wu, F., Lovorn, T., Tutuc, E. & MacDonald, A. H. Hubbard model physics in transition metal dichalcogenide moiré bands. *Phys. Rev. Lett.* **121**, 026402 (2018).
- Wang, L. et al. Correlated electronic phases in twisted bilayer transition metal dichalcogenides. *Nat. Mater.* **19**, 861–866 (2020).
- Tang, Y. et al. Simulation of Hubbard model physics in WSe₂/WS₂ moiré superlattices. *Nature* **579**, 353–358 (2020).
- Shimazaki, Y. et al. Strongly correlated electrons and hybrid excitons in a moiré heterostructure. *Nature* **580**, 472–477 (2020).
- Regan, E. C. et al. Mott and generalized Wigner crystal states in WSe₂/WS₂ moiré superlattices. *Nature* **579**, 359–363 (2020).
- Jin, C. et al. Stripe phases in WSe₂/WS₂ moiré superlattices. *Nat. Mater.* **20**, 940–944 (2021).
- Xu, Y. et al. Correlated insulating states at fractional fillings of moiré superlattices. *Nature* **587**, 214–218 (2020).
- Huang, X. et al. Correlated insulating states at fractional fillings of the WS₂/WSe₂ moiré lattice. *Nat. Phys.* **17**, 715–719 (2021).
- Chu, Z. et al. Nanoscale conductivity imaging of correlated electronic states in WSe₂/WS₂ moiré superlattices. *Phys. Rev. Lett.* **125**, 186803 (2020).
- Liu, X. et al. Tunable spin-polarized correlated states in twisted double bilayer graphene. *Nature* **583**, 221–225 (2020).
- Lu, X. et al. Superconductors, orbital magnets and correlated states in magic-angle bilayer graphene. *Nature* **574**, 653–657 (2019).
- Cao, Y. et al. Correlated insulator behaviour at half-filling in magic-angle graphene superlattices. *Nature* **556**, 80–84 (2018).
- Zondiner, U. et al. Cascade of phase transitions and Dirac revivals in magic-angle graphene. *Nature* **582**, 203–208 (2020).
- Cao, Y. et al. Tunable correlated states and spin-polarized phases in twisted bilayer–bilayer graphene. *Nature* **583**, 215–220 (2020).
- Chen, G. et al. Evidence of a gate-tunable Mott insulator in a trilayer graphene moiré superlattice. *Nat. Phys.* **15**, 237–241 (2019).
- Slagle, K. & Fu, L. Charge transfer excitations, pair density waves, and superconductivity in moiré materials. *Phys. Rev. B* **102**, 235423 (2020).
- Zhang, Y., Yuan, N. F. & Fu, L. Moiré quantum chemistry: charge transfer in transition metal dichalcogenide superlattices. *Phys. Rev. B* **102**, 201115 (2020).
- Li, H. et al. Imaging moiré flat bands in three-dimensional reconstructed WSe₂/WS₂ superlattices. *Nat. Mater.* **20**, 945–950 (2021).
- Zhang, C. et al. Probing critical point energies of transition metal dichalcogenides: surprising indirect gap of single layer WSe₂. *Nano Lett.* **15**, 6494–6500 (2015).
- Jung, S. et al. Evolution of microscopic localization in graphene in a magnetic field from scattering resonances to quantum dots. *Nat. Phys.* **7**, 245–251 (2011).
- Pradhan, N. A., Liu, N., Silien, C. & Ho, W. Atomic scale conductance induced by single impurity charging. *Phys. Rev. Lett.* **94**, 076801 (2005).
- Brar, V. W. et al. Gate-controlled ionization and screening of cobalt adatoms on a graphene surface. *Nat. Phys.* **7**, 43–47 (2011).
- Wong, D. et al. Characterization and manipulation of individual defects in insulating hexagonal boron nitride using scanning tunnelling microscopy. *Nat. Nanotechnol.* **10**, 949–953 (2015).
- Teichmann, K. et al. Controlled charge switching on a single donor with a scanning tunneling microscope. *Phys. Rev. Lett.* **101**, 076103 (2008).
- Geick, R., Perry, C. & Rupprecht, G. Normal modes in hexagonal boron nitride. *Phys. Rev.* **146**, 543–547 (1966).

Publisher's note Springer Nature remains neutral with regard to jurisdictional claims in published maps and institutional affiliations.

© The Author(s), under exclusive licence to Springer Nature Limited 2021

Data availability

Source data are available for this paper at https://github.com/HongyuanLiCMP/Moire_discharging_STM_data. All other data that support the findings of this paper are available from the corresponding authors upon request.

Acknowledgements

This work was funded by the US Department of Energy, Office of Science, Office of Basic Energy Sciences, Materials Sciences and Engineering Division, under contract no. DE-AC02-05-CH11231 (van der Waals heterostructure programme KCFW16) (device electrode preparation, STM spectroscopy, DFT calculations and theoretical analysis). Support was also provided by the US Army Research Office under MURI award W911NF-17-1-0312 (device layer transfer), by the National Science Foundation award DMR-1926004 (structural determination) and by the National Science Foundation award DMR-1807233 (surface preparation). S.T. acknowledges support from DOE-SC0020653 (materials synthesis), Applied Materials Inc., NSF CMMI 1825594 (NMR and TEM studies), NSF DMR-1955889 (magnetic measurements), NSF CMMI-1933214, NSF 1904716, NSF 1935994, NSF ECCS 2052527, DMR 2111812 and CMMI 2129412. K.W. and T.T. acknowledge support from the Elemental Strategy Initiative conducted by MEXT, Japan, grant number JPMXP0112101001; JSPS KAKENHI grant number JP20H00354; and CREST (JPMJCR15F3), JST, for bulk hBN crystal growth and analysis. E.R. acknowledges support from the Department of Defense (DoD) through the National Defense Science and Engineering Graduate Fellowship (NDSEG) programme. S.L. acknowledges support from Kavli ENSI Heising-Simons Junior Fellowship. M.H.N.

thanks S. Kundu and M. Jain for their implementation of non-collinear wave-function plotting in Siesta.

Author contributions

F.W. and M.F.C. conceived the project. S.G.L. supervised the theoretical calculations. H.L. and S.L. performed the STM measurement. M.H.N. carried out the DFT calculations. H.L., J.X., X.L., W.Z., E.R. and D.W. fabricated the heterostructure device and performed the second harmonic generation measurement. K.Y., M.B. and S.T. grew the WSe₂ and WS₂ crystals. K.W. and T.T. grew the hBN single crystal. All the authors discussed the results and wrote the manuscript.

Competing interests

The authors declare no competing interests.

Additional information

Supplementary information The online version contains supplementary material available at <https://doi.org/10.1038/s41567-021-01324-x>.

Correspondence and requests for materials should be addressed to S.L., M.F.C. or F.W.

Peer review information *Nature Physics* thanks Kam Tuen Law and the other, anonymous, reviewer(s) for their contribution to the peer review of this work.

Reprints and permissions information is available at www.nature.com/reprints.